Optical properties of meteoric smoke analogues

Tasha Aylett[1], James S. A. Brooke[1], Alexander D. James[1], Mario Nachbar[2], Denis Duft[2], Thomas Leisner[2,3], John M. C. Plane[1]

(1) School of Chemistry, University of Leeds, Leeds, UK.

(2) Institute for Meteorology and Climate Research, Karlsruhe Institute of Technology (KIT), Karlsruhe, Germany

(3) Institute of Environmental Physics (IUP), Ruprecht-Karls-University Heidelberg, Heidelberg, Germany

Abstract

Accurate determination of the optical properties of analogues for meteoric smoke particles (MSPs), which are thought to be composed of iron-rich oxides or silicates, is important for their observation and characterization in the atmosphere. In this study, a photochemical aerosol flow reactor (PAFS) has been used to measure the optical extinction of iron oxide MSP analogues in the wavelength range 325-675 nm. The particles were made photochemically, and agglomerate into fractal-like particles with sizes on the order of 100 nm. Analysis using Transmission Electron Microscopy (TEM), Energy Dispersive X-ray spectroscopy (EDX) and Electron Energy Loss Spectroscopy (EELS) suggested the particles were most likely maghemite-like (γ-Fe_2O_3) in composition, though a magnetite-like composition could not be completely ruled out. Assuming a maghemite-like composition, the optical extinction coefficients measured using the PAFS were combined with maghemite absorption coefficients measured using a complementary

22   experimental system (the MICE-TRAPS) to derive complex refractive indices that reproduce

23   both the measured absorption and extinction.

24

1. Introduction

26   The ablation of cosmic material in the mesosphere leads to the formation of nanometer-sized
27   meteoric smoke particles (MSPs) (Plane et al., 2015). Reaction, condensation and subsequent
28   agglomeration of stable reservoir species such as FeOH, $Mg(OH)_2$, $NaHCO_3$ and SiO_2 leads to
29   the formation of MSPs over a timescale of several days. However, very little is known about the
30   physical and chemical properties of these particles. It is important to establish the composition
31   and other characteristics of MSPs because the particles are thought to be involved in a wide
32   range of atmospheric processes as they are transported down through the atmosphere, including:
33   mesospheric metal chemistry; mesospheric oxygen chemistry; nucleation of polar mesospheric
34   clouds (PMCs); stratospheric aerosol chemistry (including the nucleation of polar stratospheric
35   clouds (PSCs)); and deposition of bioavailable metal sulfates into the oceans (Plane et al., 2015).

36   The detection and characterisation of MSPs has proven extremely challenging as the
37   mesosphere-lower thermosphere (MLT) is a notoriously difficult region in which to perform in
38   situ studies. In terms of the composition, at present only two types of investigations exist: rocket-
39   borne instruments (e.g. Faraday cup detectors and electric work-function studies) and remote
40   sensing (e.g. optical spectroscopy). The only direct measurements have been obtained *via*
41   sounding rocket flights, though only charged particles have been sampled with any success. One
42   example is the ECOMA (Existence and Charge state Of Meteoric smoke particles in the middle
43   Atmosphere) project (Rapp et al., 2010). This work constrained the MSP size and work function,
44   with electronic structure calculations inferring a likely MSP composition of Fe and Mg
45   hydroxide clusters with low silica content (Rapp et al., 2012).

46   Important progress has also been achieved using remote sensing techniques: the SOFIE (Solar
47   Occultation for Ice Experiment) instrument on the AIM (Aeronomy of Ice in the Mesosphere)
48   satellite has detected MSPs by optical extinction, conducting solar occultation measurements
49   from April 2007 to the present. Extinction measurements at 330, 867 and 1037 nm were used to
50   show that the best-fit particle compositions are iron-rich oxides (magnetite (Fe_3O_4), wüstite
51   (FeO), magnesiowüstite ($Mg_xFe_{1-x}O$, x=0 -0.6)) or iron-rich olivine ($Mg_{2x}Fe_{2-2x}SiO_4$, x=0.4-0.5)
52   (Hervig et al., 2017). That is, the major meteoric elements Fe, Mg and Si are either mixed in
53   olivinic particles with a single average composition, or MSPs are a mix of metal oxide and silica
54   particles. However, this technique makes an important assumption: that the bulk (crystalline)
55   refractive indices (RIs) used to infer smoke compositions are applicable to MSPs, despite
56   evidence that the particles are structurally amorphous, fractal-like agglomerates (Saunders and
57   Plane, 2006). This assumption is currently not confirmed, and as such it is important to measure
58   RIs of realistic MSP analogues, especially those of iron-rich particles.

59   A number of crystalline MSP analogues (Fe_2O_3, silica (SiO_2) and iron silicates ($Fe_xSi_{(1-x)}O_3$ ($0 \leq$
60    $x \leq 1$))) with radii on the order of 2 nm have recently been generated in the laboratory using a
61   low pressure, non-thermal microwave resonator (Nachbar et al., 2018a;Nachbar et al., 2018c).
62   The particles are transferred to a low pressure, supersaturated particle trap - the Molecular Flow

63   Ice Cell/Trapped Reactive Atmospheric Particle Spectrometer (MICE/TRAPS) - in which
64   particle properties can be determined. The latest work using this system derived absorption
65   efficiencies for Fe_2O_3 particles at 450, 488 and 660 nm (Nachbar et al., 2018c). David et al.
66   (2012) have demonstrated the production of maghemite particles with a similar experimental
67   arrangement. In fact, Navrotsky et al. (2008) have argued that maghemite is thermodynamically
68   favored with respect to hematite for particles smaller than 16 nm in diameter. The particles
69   produced in the study of Nachbar et al. (2018b) are therefore very likely to have been
70   maghemite.

71   Amorphous MSP analogues have previously been generated in the laboratory using a
72   photochemical aerosol flow system (PAFS) (Saunders and Plane, 2011, 2010, 2006). Particles
73   with compositions close to the minerals hematite (α-Fe_2O_3), goethite (FeOOH), fayalite
74   (Fe_2SiO_4) and silica (SiO_2) were produced when metal-containing precursors were photolysed in
75   the presence of O_3/O_2. Particle size distributions were measured using a Scanning Mobility
76   Particle Sizer (SMPS), and optical extinction measurements were obtained for comparison with
77   values calculated from Mie theory using literature RIs for the unidentified particles. Although the
78   experimental size distributions of the MSP analogues produced could be replicated using an
79   agglomeration model (Jacobson, 2005;Saunders and Plane, 2010, 2006), there was significant
80   uncertainty in the measured size distribution. Consequently, Mie theory was able to reproduce
81   the measured extinction using bulk RIs for α-Fe_2O_3 and Fe_2SiO_4 particles, though not when using
82   the experimental size distribution.

83   In this manuscript, the photochemical technique used by Saunders and Plane has been developed
84   further to study the agglomeration and optical properties of iron oxide particles. The measured
85   optical extinction has been modelled using Mie theory and the Rayleigh-Debye-Gans (RDG)
86   approximation (discussed below). Analysis using Transmission electron microscopy (TEM),
87   Electron Energy Loss Spectroscopy (EELS) and EDX (Energy Dispersive Xray) spectroscopy
88   indicate a maghemite-like (γ-Fe_2O_3) particle composition. The measured optical extinction data
89   was combined with absorption efficiencies from Nachbar et al. (2018c) to derive wavelength-
90   dependent complex RIs that reproduce the measured extinction. Maghemite particles have not
91   been previously considered in the compositional analysis of MSPs because no RIs are available
92   in the literature. However, the formation of maghemite nanoparticles in laboratory studies *via*
93   two different production methods (*via* photolysis/in microwave plasma) that operate under
94   distinctly different conditions demonstrates the potential relevance of this species in the
95   atmosphere, and the need for further studies on this compound as a potential candidate for MSPs.

96

97   **2. Experimental Methods**

98   **2.1 PAFS**

99   The photochemical apparatus used to generate analogue MSPs (Figure 1) has been described
100   previously (Saunders and Plane, 2006, 2010, 2011). The setup consists of a cylindrical glass
101   photolysis cell with quartz end windows ($r = 4$ cm; $\phi = 25$ cm) into which a combined flow of
102   the Fe precursor, iron pentacarbonyl vapour ($Fe(CO)_5$), and O_3/O_2 was introduced. The $Fe(CO)_5$
103   was generated by passing a flow of N_2 through a round-bottomed flask containing ~3 cm^3 of
104   liquid $Fe(CO)_5$ (Aldrich) cooled in a water-ice bath to 0 °C. The round-bottomed flask and ice-
105   bath were covered to prevent any premature photolysis (and subsequent build-up of material on
106   the flow tube walls). O_3 was produced by photolysing O_2 at 184 nm, by passing a flow of O_2

107 through a glass cell with a quartz window in front of a Hg pen lamp. Once in the photolysis cell,
108 the gases were irradiated using a 1000 W ozone-free Xenon arc lamp. Variable N_2 'curtain'
109 flows were passed across each of the cell windows such that the total flow rate was 550 sccm (1
110 sccm = 1 cm^3 min^{-1} at standard temperature and pressure (273 K and 1 bar)). After leaving the
111 photolysis cell the particle flow was directed through an absorption cell ($r = 10$ cm; $\phi = 48$ cm)
112 with White cell optics in which the optical extinction of the particles was measured (hereafter
113 referred to as the White cell). On exit from the White cell, particle size distributions were
114 recorded using a SMPS consisting of a differential mobility analyser (DMA) and a condensation
115 particle counter (CPC). The DMA sheath and aerosol flow rates were 3 L min^{-1} and 0.3 L min^{-1}
116 respectively, with a scan taken every 3 minutes (a scan time of 120 seconds and retrace of 30 s
117 was used).

118
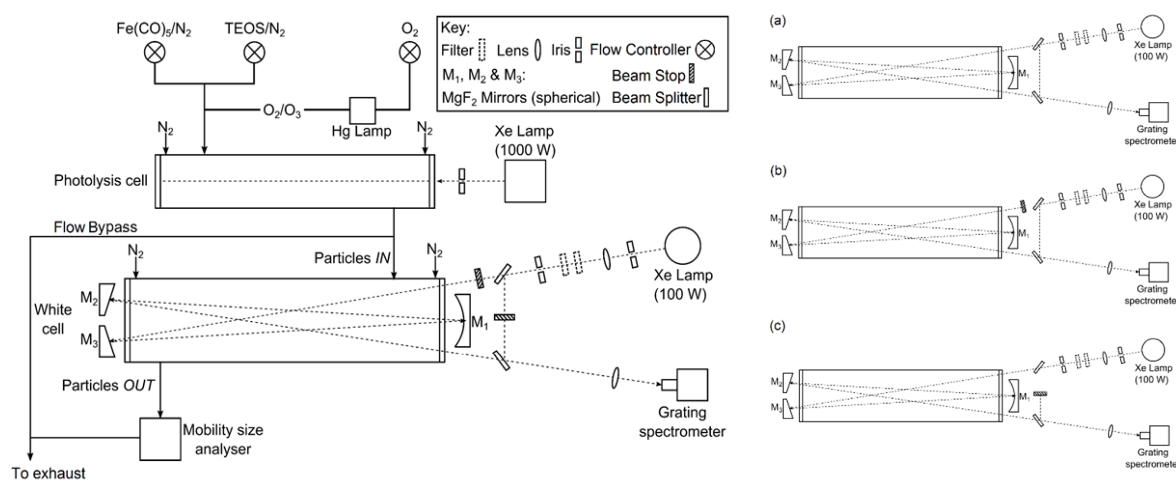
119

120 Figure 1. Schematic diagram of the experimental system used for the generation and optical detection of
121 MSP analogues, where a, b & c show different beam configurations used to generate a normalised cell
122 spectrum.

123 Light from a 100W Xenon arc lamp was focused into the cell using a quartz lens (focal length =
124 75 cm). The lamp intensity could be controlled by the insertion of a selection of neutral density
125 filters, and stray lamp light was eliminated using an iris. Borosilicate White cell windows
126 prevented further photolysis by the spectroscopy lamp, and excluded second-order light at
127 wavelengths below ~330 nm from entering the spectrometer and potentially contaminating the
128 spectra. N_2 curtain flows (500 sccm) were passed across the windows to prevent aerosol
129 deposition. Particle extinction was measured between 325 and 675 nm. A total optical path
130 length (l) of 624 cm was achieved by folding the light path 12 times between three concave
131 mirrors comprising the White cell. The exit beam was focused with a quartz lens onto a fibre
132 optic coupled to an Acton Research Spectra Pro 500i spectrometer, in which the light was
133 dispersed using a grating (150 groove mm^{-1}) onto a CCD camera. The exposure time was 0.1 s,
134 with 57 accumulations per spectrum generating 9 spectra per minute.

135 To measure smaller levels of optical extinction than in our previous work (Saunders and Plane,
136 2006, 2010, 2011), an optical by-pass was introduced to normalize for drifts in the Xe lamp
137 spectral intensity with time. Beam stops were used to create three different beam configurations
138 from which the separate signals could be extracted (Figure 1). Spectra were recorded in three

139 minute cycles with one minute of spectra taken using each configuration: (a) the beam directed
140 through the cell and additionally through the bypass (I_a); (b) the beam directed only through the
141 bypass (I_b); and (c) the beam directed only through the cell (I_c). This generated one normalized
142 spectrum (I_n) every three minutes (see equation E1). The minimum detectable absorbance ranged
143 from 0.07 to 0.004 over the wavelength range studied.

144 E1 $$(I_n(\lambda) = \big(I_a(\lambda) - I_b(\lambda)\big)/\big(I_a(\lambda) - I_c(\lambda)\big),$$

145 In a typical experiment, the sample flows were switched on, with the particle flow initially
146 diverted to an exhaust rather than through the White cell. The background particle size
147 distribution and optical intensity in the White cell ($I_{n,bg}(\lambda, t)$) were then measured for about 30
148 minutes. The particle flow was then directed through the White cell, and a further 21 minutes of
149 sample measurements were recorded ($I_{n,sa}(\lambda, t)$). Thereafter, the particle flow was diverted back
150 to the exhaust and background measurements resumed for around 45 minutes. A repeat sample
151 measurement was recorded followed by approximately 30 minutes of reference measurements
152 until the peak of the recorded size distribution had stabilized to within 1 %.

153 The gas-phase spectrum for the Fe(CO)$_5$ precursor was measured with a PerkinElmer Lamda 90
154 UV/Vis spectrometer in a 1 × 1 cm gas cuvette. Due to the wide range covered by the absorption
155 cross section in the measured wavelength range (4 orders of magnitude), the final spectrum was a
156 composite of two spectra; the low-wavelength end of the spectrum ($\lambda < 280$ nm) was an average
157 of three low pressure measurements (P ~ 2 torr) and the high wavelength portion ($\lambda > 280$ nm)
158 was an average of two higher pressure measurements (P ~ 20-30 torr). A reference spectrum for
159 the empty cuvette was subtracted from each individual spectrum before averaging.

160

161 **2.2 TEM**

162 Particles formed in the photochemical aerosol flow system were collected by diverting the flow
163 bypass through a round-bottomed flask containing a suspended transmission electron microscopy
164 (TEM) grid (copper mesh with a holey carbon film coating). The grids were then stored under
165 vacuum in the dark prior to imaging. Particles were analysed using TEM with energy dispersive
166 X-ray spectroscopy (EDX) and electron energy loss spectroscopy (EELS) at the University of
167 Leeds (FEI Titan3 Themis 300).

168

169 **2.3 MICE/TRAPS**

170 Absorption efficiencies determined in Nachbar et al. (2018c) for maghemite particles with the
171 MICE/TRAPS apparatus were used in combination with the optical extinction measured in this
172 work for iron oxide particles produced with the PAFS apparatus, in order to derive complex RIs.
173 The experimental and analytical methods used for the MICE/TRAPS experiment have been
174 described in detail previously (Meinen et al., 2010a; Meinen et al., 2010b; Duft et al., 2015;
175 Nachbar et al., 2016), with the recent methodology for particle production outlined in Nachbar et
176 al. (2018a). The analysis procedure for the determination of absorption efficiencies is specified
177 in Nachbar et al. (2018c).

178 In brief, singly charged, spherical and compact nanoparticles are produced by mixing vapour
179 from a volatile precursor (solid ferrocene, Fe(C$_5$H$_5$)$_2$, ~353 K) with a flow of oxygen and helium.
180 This mixture then flows through a low pressure, non-thermal microwave resonator to create a

181 plasma in which metastable exited Fe is oxidised to produce Fe_2O_3 particles. A portion of the
182 flow passes into a vacuum chamber through an aerodynamic lens, a flow-limiting orifice and an
183 octupole ion guide (Figure S1, supplementary information). Particles of a chosen size are
184 deflected with a quadrupole deflector and are subsequently trapped into a cloud of ~ 1 mm radius
185 within the ion trap MICE, where a He bath gas is added to thermalize the particles. Within the
186 MICE, the particles are subject to a well calibrated concentration of gas phase H_2O molecules
187 (Nachbar et al., 2018b). Small numbers of particles are extracted from the trap at regular time
188 intervals to a Time-of-Flight (ToF) mass spectrometer for particle mass determination.

189 In a typical experimental run, Fe_2O_3 particles were admitted into the MICE, where H_2O
190 molecules were adsorbed onto the particle surfaces with increasing trapping time until an
191 equilibrium of adsorbing and desorbing molecules was reached. A number of repeat runs were
192 performed where the cloud of particles was irradiated using optically pumped continuous wave
193 semiconductor lasers (OBIS LX, Coherent, at 405 nm, 488 nm and 660 nm), increasing the laser
194 power in each subsequent run. Absorption of the laser light by the particles caused heating and
195 desorption of H_2O molecules from the particle surface (see Figure S2, supplementary
196 information). Parameters such as the initial mass and radius (r) of the particles, and the
197 temperature change due to irradiation could then be calculated from the mass of the levitated
198 nanoparticles as a function of the residence time in MICE. Assuming an equilibrium between
199 radiative heating and collisional cooling enables the absorption cross section (C_{abs}), and
200 absorption efficiency (Q_{abs}, see equation E2) to be calculated. The latter is typically used when
201 comparing the absorption of different sized particles.

202 E2
$$Q_{abs} = \frac{C_{abs}}{\pi \cdot r^2}$$

203

3. Results and Discussion

3.1 TEM

206 Examination of particles collected from the PAFS using TEM show non-spherical, fractal-like
207 particles. A range of particle sizes can be observed, ranging from tens of nanometers to microns
208 in radius (Figure 2). The fractal-like agglomerates are formed of primary spheres, whose size
209 was estimated by taking a number of measurements from three high resolution images of
210 different agglomerates, one of which is shown in Figure 2 (right-hand panel). In each of these
211 three images, 15 primary spheres were measured from around the visible 'edge' of the particle,
212 where a defined spherical shape could be seen. This analysis resulted in a primary particle radius
213 of 1.65 ± 0.15 nm.
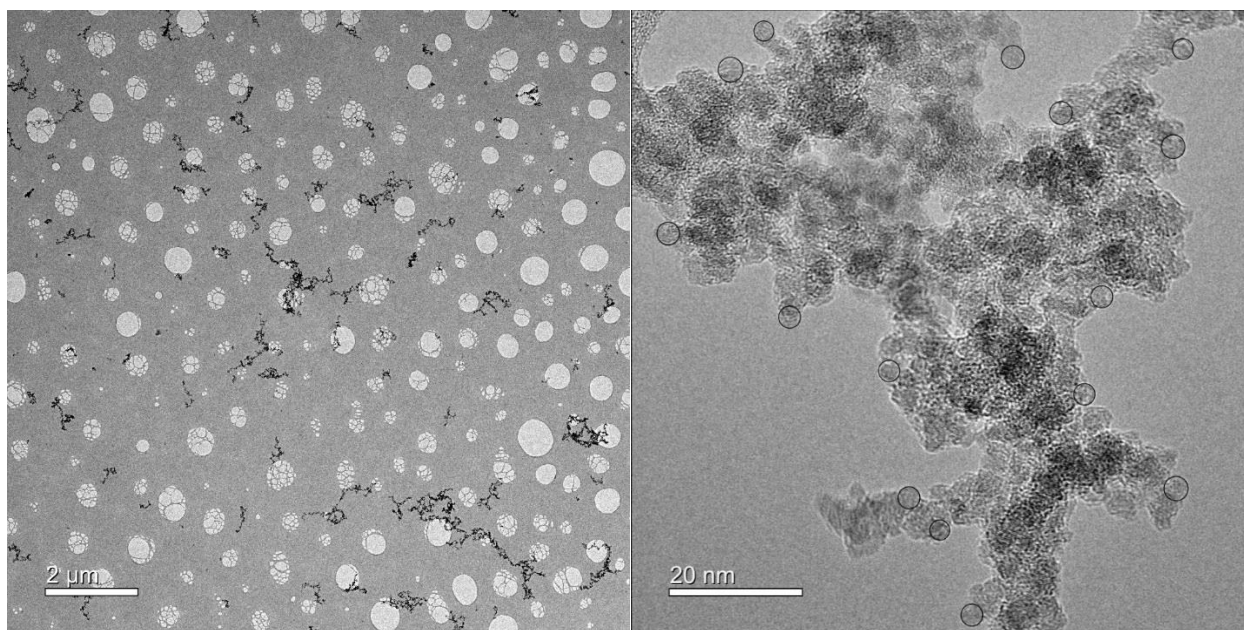
214

215 Figure 2. (Left panel) Low resolution TEM image showing the size-range of iron oxide agglomerates (dark
216 grey/black particles) collected on a holey-carbon grid (light grey holes and webbing). (Right panel) High
217 resolution TEM image showing the primary particles forming an agglomerate. Black circles indicate
218 measured primary spheres used for size characterisation.

219

220 Comparison of the background-subtracted, low-loss deconvolved Fe L-edge and O K-edge EELS
221 spectra with those from iron oxide standards can provide information on the particle composition
222 (Figure 3, left-hand panels) (Brown et al., 2017; Brown et al., 2001). The O K-edge spectra for
223 the iron oxide standards have been aligned using the energy loss for the peak designated as *b* in
224 Figure 3, due to the invariance of this peak in the spectra. Likewise, the Fe L-edge spectra have
225 been aligned to the sample peak *a*. On inspection of the O K-edge, a wüstite-like sample
226 composition can be excluded due to the differing edge-onset energy and shape of peak *a*. A
227 hematite-like sample composition can also be rejected on the basis of the lack of the double-peak
228 structure characteristic of hematite in the sample spectrum. This is corroborated on inspection of
229 the Fe L-edge, where a well-defined shoulder on the low energy side and a broad shoulder on the
230 high energy side of peak *a* are observed for hematite and wüstite, respectively, neither of which
231 are present in the sample spectrum.

232 In the case of both magnetite and maghemite there are no distinctive features in either the O K or
233 Fe L-edges to easily distinguish between the two species. Nonetheless, upon closer inspection
234 (Figure 3, right-hand panels) the sample spectra more closely resemble those for the maghemite
235 standard as compared to those for magnetite. For the Fe L-edge, although the shoulder on the low
236 energy side of peak *a* is larger in the sample spectrum than that observed for maghemite, it is
237 more well defined than the shoulder seen in the magnetite spectrum. Furthermore, the profile of
238 peak *a* more closely follows that for the maghemite standard on both the high and low energy
239 sides. Though a defined double-peak structure is not observed in peak *b*, both the peak profile on
240 the high energy side and the height of the peak more closely resemble maghemite. For the O K-
241 edge, although there are some differences between the sample spectra and those for both
242 standards (notably the lack of a defined peak *c*), there are minimal differences between the

243 spectra for the maghemite and magnetite standards. For this reason, though the profile of peak *a*
244 more closely follows that of maghemite, it is not possible to distinguish between the two species
245 from the O K-edge spectra alone.

246
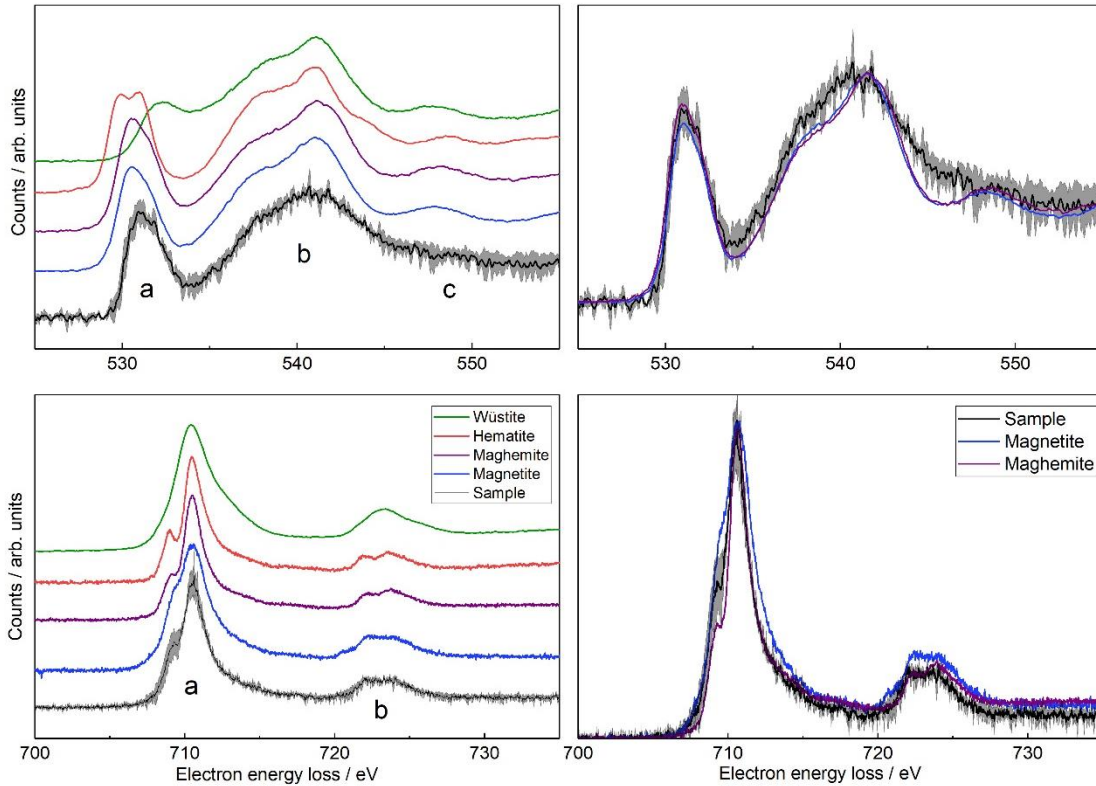
247

248 Figure 3. Electron energy loss spectra measured with the TEM compared to spectra for iron oxide standards
249 (Brown et al., 2017; Brown et al., 2001). Top panels: O K-edge. Bottom panels: Fe L edge. Grey shaded
250 regions indicate the experimental uncertainty. The left-hand panels show the spectra offset for clarity, and
251 the right-hand panels show the same spectra (for the sample, magnetite and maghemite) superimposed.

252

253 The defined peak *c* is not observed in the sample O K-edge, which we speculate may be due to the
254 poor crystallinity of the particles. This is confirmed by the electron diffraction pattern (Figure S3,
255 supplementary information) where two broad rings are observed coinciding with the intense
256 reflections of magnetite/maghemite. The interplanar distances measured, accounting for a camera
257 calibration error of ± 6 %, were 2.60 Å and 1.47 Å near to the 311 and 440 diffraction planes,
258 respectively (cf. measured distances of 2.57 Å and 1.52 Å in a maghemite standard). A faint ring
259 was observed at an interplanar distance of 2.09 Å, close to the 400 diffraction plane at 2.11 Å. The
260 diffraction pattern cannot distinguish between maghemite and magnetite, since both are based on
261 a spinel crystal structure. However, this analysis does corroborate that the sample composition is
262 very similar to one or other of these minerals. Elemental quantification using EELS resulted in a
263 Fe/O ratio of 0.48 ± 0.12 – more oxygen rich than any of the possible compositions
264 hematite/maghemite, magnetite or wüstite (the oxides have Fe/O ratios of 0.67, 0.75 and 1,
265 respectively, i.e. Fe:O = 2:3, 3:4 and 1:1). As such, the composition is most likely to be maghemite-

266 like, although potentially with additional oxidation or oxygen contamination. This additional
267 oxygen could be another reason for the differences observed in the O K-edge.

268 The Energy Dispersive X-ray (EDX) spectrum (Figure S4, supplementary information) confirms
269 the presence of Fe and O, though some differences are observed in the intensities of the peaks in
270 the spectra for the agglomerate and the maghemite standard. In the agglomerate spectrum, the
271 intensity of the low energy Fe L-peak is higher than for the standard, which we speculate may be
272 due to fluorescence from excited Cu X-rays from a grid bar, consistent with a relatively large
273 amount of Cu in the agglomerate spectrum. The sample is also more oxygen-rich than the standard.
274 This could result from contamination which was introduced after deposition, prior to TEM
275 imaging. A significant carbon peak is observed in the agglomerate spectrum, suggesting a possible
276 C and O rich hydrocarbon source for this contamination. Alternatively, oxygen could have been
277 introduced within the flow apparatus, by coordination to, or reaction with, an oxygen-rich species
278 O_3, forming an oxide coating.

279 FeO_3 is thought to form from the sequential oxidation of Fe by O_3 (Fe → FeO → FeO_2 → FeO_3);
280 the rate coefficients for these three reaction have been measured in the gas phase to be fast (Self
281 and Plane, 2003). The formation of Fe_2O_3 smoke analogues in the PAFS apparatus has been
282 previously proposed to occur by polymerization and subsequent re-ordering of FeO_3 in the solid
283 phase (Saunders and Plane, 2006); it may be that incomplete re-structuring of the FeO_3 has
284 occurred, thus causing the decreased Fe/O ratio. Previous work using the PAFS under comparable
285 experimental conditions obtained a Fe/O ratio of 0.65 ± 0.06 (Saunders and Plane, 2006). Although
286 this was suggested to imply the formation of hematite, it would also be consistent with maghemite.
287 Navrotsky et al. (2008) show that for nanoparticles less than ~16 nm in size, maghemite is more
288 stable than hematite since it has a lower surface enthalpy. We therefore conclude that a maghemite-
289 like composition is most likely for the smoke analogues generated using the PAFS.

290

3.2 PAFS

292 The reduction in intensity of a beam of light from I_0 to I as it traverses a distance l through an
293 absorbing medium can be expressed as an optical density (OD) using the Beer-Lambert equation:

294 E3
$$OD = ln\left(\frac{I_0}{I}\right) = \alpha_{ext} \cdot l$$

295 where the extinction coefficient α_{ext} arises from both absorption and scattering. The intensity (I)
296 at time t is given by the sample spectrum recorded with the particle flow directed through the
297 absorption cell ($I_{n,sa}(\lambda, t)$). A straight line reference fitted to the background spectrum ($I_{n,bg}(\lambda, t)$)
298 yields I_0 at time t, enabling the time and wavelength-dependent OD to be extracted from the raw
299 spectra. Once the particle size distribution exiting the absorption cell of the PAFS had stabilized,
300 spectra were averaged to obtain one OD spectrum for the iron oxide nanoparticles (Figure 4). As
301 shown by the black shaded area in the bottom panel of Figure 4, the uncertainty in the OD
302 increased significantly at small wavelengths as a result of the decreasing intensity of the
303 spectroscopic lamp and the fall-off in quantum efficiency of the CCD detector. Consequently,
304 the optical data below 350 nm was discarded. At long wavelengths, data above 550 nm was also
305 discarded because the OD decreased below the detection limit. The OD spectrum was also
306 corrected for contributions from the residual precursors used to make the particles. The OD of
307 residual O_3 was negligible over the wavelength range of usable experimental data ($\lambda > 350$ nm).

308 However, the residual Fe(CO)$_5$ spectrum did need to be subtracted. Inspection of the literature
309 did not yield appropriate data, so the Fe(CO)$_5$ absorption cross section was measured (Figure 6,
310 top panel). The cross section data is listed in Table S3. The extent of Fe(CO)$_5$ photolysis in the
311 photolysis cell (Figure 1) was calculated using the flow rates, the lamp irradiance and the
312 wavelength-dependent absorption cross sections.
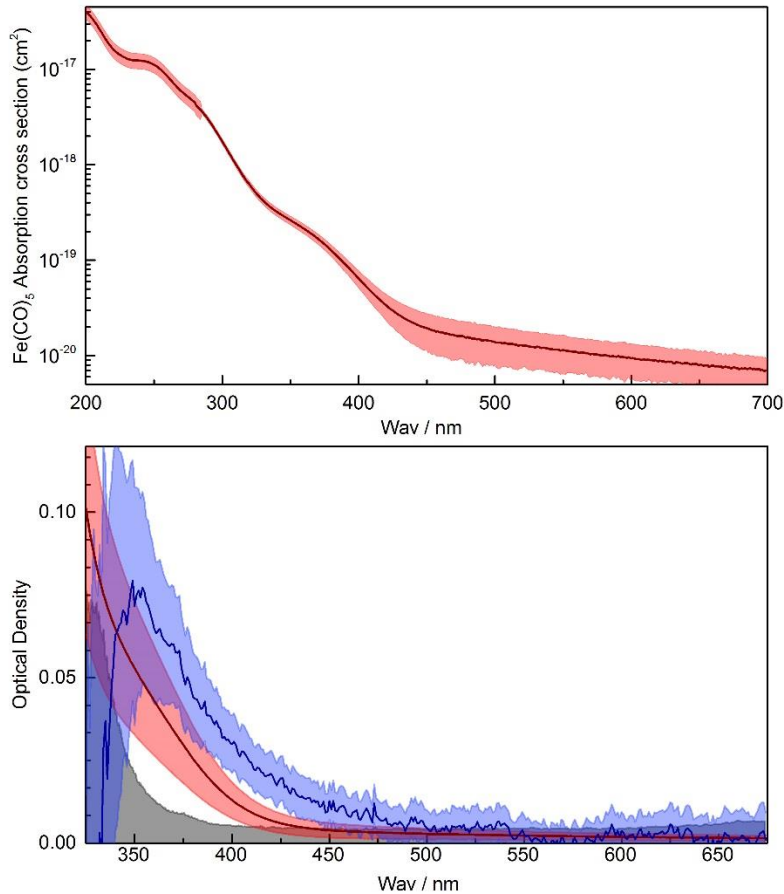
313

314 Figure 4. Top panel: Measured Fe(CO)$_5$ absorption cross section (cm^2) with experimental uncertainty
315 indicated by red shading. Bottom panel: Iron oxide particle extinction with the precursor spectrum removed
316 (blue line) and experimental uncertainty indicated by light blue shading. Also shown is the spectrum for
317 the Fe(CO)$_5$ present in the absorption cell (red line), with the experimental uncertainty indicated by red
318 shading. The detection limit for the experiment is shown with the black line and shaded region. Note the
319 different wavelength ranges in each panel.

320

321 The size distribution of agglomerates measured with the SMPS follows an approximate
322 lognormal distribution peaking around 100 nm radius (demonstrated by the lognormal fit in
323 Figure 5). A small additional mode is present in the distribution with a peak of approximately 30
324 nm. The measured size distribution provides a measure of the mobility radius, which is not
325 necessarily equivalent to the fractal (outer) radius of amorphous particles – these are typically
326 sized differently to spherical particles in an SMPS as they experience higher drag compared to a
327 sphere with the same mass (DeCarlo et al., 2004). As such, it should be noted that it may not be
328 appropriate to use the measured size distribution to calculate the optical extinction. Indeed, some

329   very large (~2 μm) particles are observed in the TEM images, though these may have resulted
330   from further agglomeration during deposition on the collection grid. As shown in Figure 6, using
331   Mie theory with the experimental size distribution over-predicts the OD by at least an order of
332   magnitude when using literature RIs for hematite, magnetite and wüstite (Hsu and Matijevic,
333   1985; Longtin et al., 1988; Querry, 1985; Fontijn et al., 1997; Huffman and Stapp, 1973;
334   Henning and Mutschke, 1997). No equivalent calculation can be performed for maghemite as the
335   bulk RIs are not available in the literature.
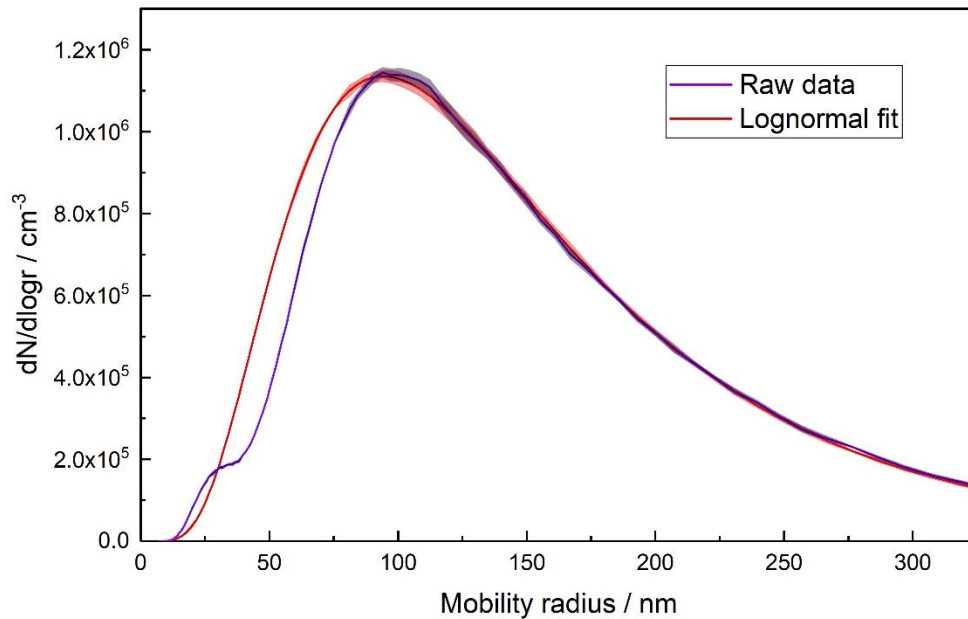
336

337   Figure 5. Measured size distribution (purple) and a lognormal fit to the experimental data (red) with shaded
338   areas indicating the experimental uncertainty.

339

340
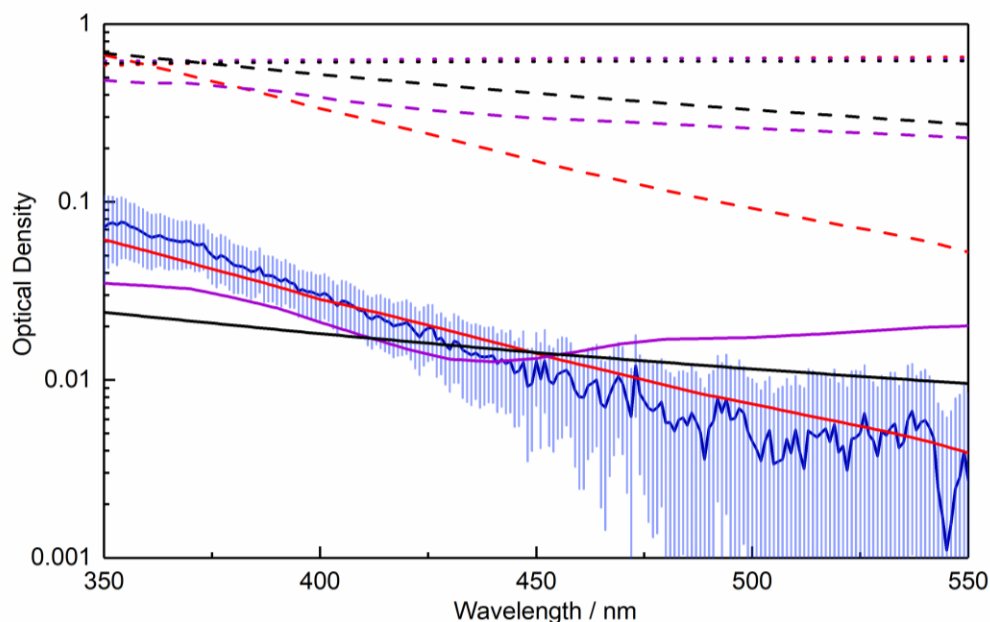
Figure 6. Measured OD as a function of wavelength (blue line), compared with the average OD calculated from literature data for hematite (red, (Hsu and Matijevic, 1985; Longtin et al., 1988; Querry, 1985)), magnetite (purple, (Fontijn et al., 1997; Huffman and Stapp, 1973; Querry, 1985)) and wüstite (black, (Henning and Mutschke, 1997)) using the measured size distribution (dotted lines), the RDG approximation with a monomer concentration derived from the measured size distribution (dashed lines) and the RDG approximation with a monomer concentration fitted to the experimental data (solid lines).

347

An alternative method for calculating the OD of amorphous agglomerates is the Rayleigh-Debye-Gans (RDG) approximation (Sorensen, 2001), where an agglomerate is treated as a monodisperse distribution of primary spheres and the overall agglomerate extinction is calculated by summing those of the individual primary particles. Using a concentration of $r =$ 1.65 nm monomers calculated by integrating the measured size distribution (4.3×10^{11} cm^{-3}), Figure 6 shows that the OD is again over-predicted by around an order of magnitude, though a decrease in OD with increasing wavelength is obtained which more closely matches the experimental data. If the monomer concentration is reduced, as would be expected if the observed size distribution is made up of fractal-like particles rather than solid spheres, significantly better fits to the experimental data can be achieved for all species considered, with the best agreement achieved when using hematite RIs (Figure 6). Assuming the RDG approximation holds, a comparison can be made with absorbance data for maghemite (Jain et al., 2009; Tang et al., 2003): for particles on the order of a few nanometers in size, absorption dominates over scattering (for the iron oxides, scattering < 0.01 % absorption). As such, the contribution from scattering to the OD can be neglected, and the absorbance data available in the literature can be arbitrarily scaled for comparison with the experimental data, since scaling the absorbance is equivalent to changing the concentration of monomers in the RDG approximation. This comparison is shown in Figure 7, where the literature data agrees reasonably well with the measured OD. As the literature optical data for hematite and maghemite best replicate the

367 measured OD, this again suggests the most likely composition to be maghemite-like, given that
368 the EELS analysis definitively excludes a hematite composition.
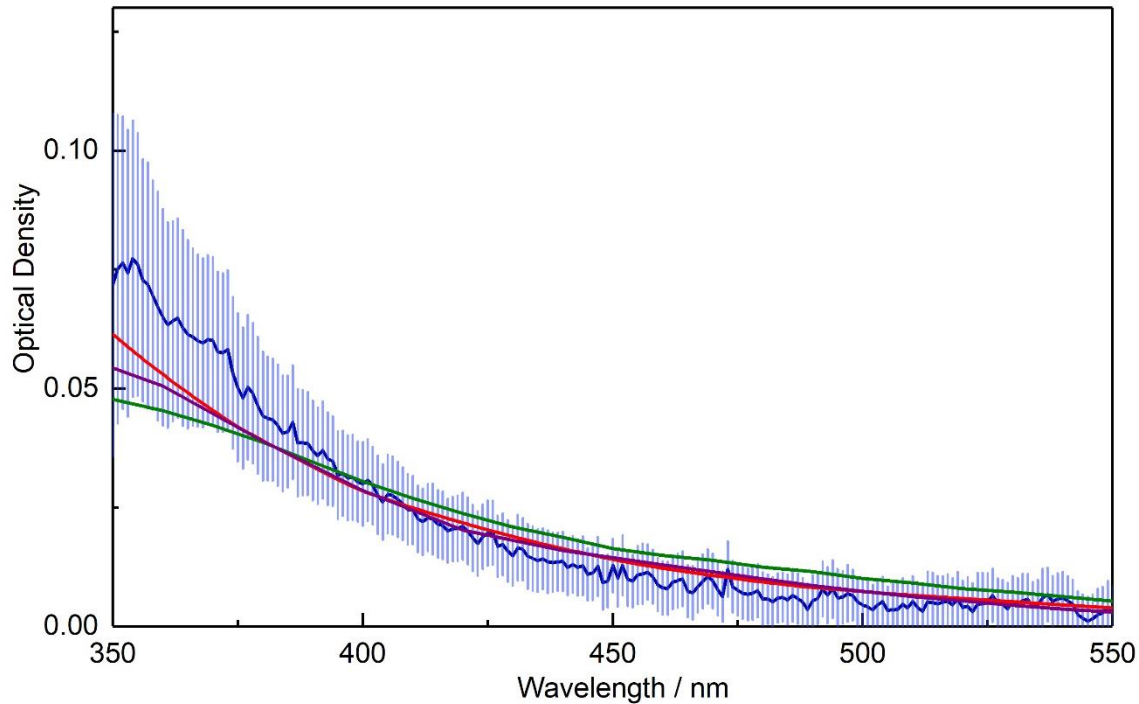
369

370

371 Figure 7. Measured OD (blue line), scaled maghemite OD from Jain et al. (2009) (green line) and scaled
372 maghemite OD from Tang et al. (2003) (purple line), as a function of wavelength. Also shown is the average
373 OD calculated from literature data for hematite (red, (Hsu and Matijevic, 1985; Longtin et al., 1988; Querry,
374 1985)) using the RDG approximation with a monomer concentration fitted to the experimental data (as
375 shown in Figure 6).

376

377 **3.3 Photochemical Modelling**

378 The previously measured size-dependent absorption efficiencies from the MICE/TRAPS
379 experiment that were used to derive complex RIs are shown in Figure 8. The solid lines represent
380 an average of the absorption efficiencies calculated with Mie theory from hematite RIs available
381 in the literature (Querry, 1985; Bedidi and Cervelle, 1993; Hsu and Matijevic, 1985; Longtin et
382 al., 1988). The experimental data generally agrees with that from the literature, given the
383 experimental uncertainties and the variation in literature values. The best agreement is seen at
384 488 nm, where there is approximately a 20 % difference between the size-dependent literature
385 average and the experimental values. The absorption efficiencies at 405 nm are around 45 %
386 larger than the average literature values, whilst still being within the spread of the experimental
387 error. Those at 660 nm are around 45 % smaller than the average literature values, on the edge of
388 the range spanned by the experimental errors.
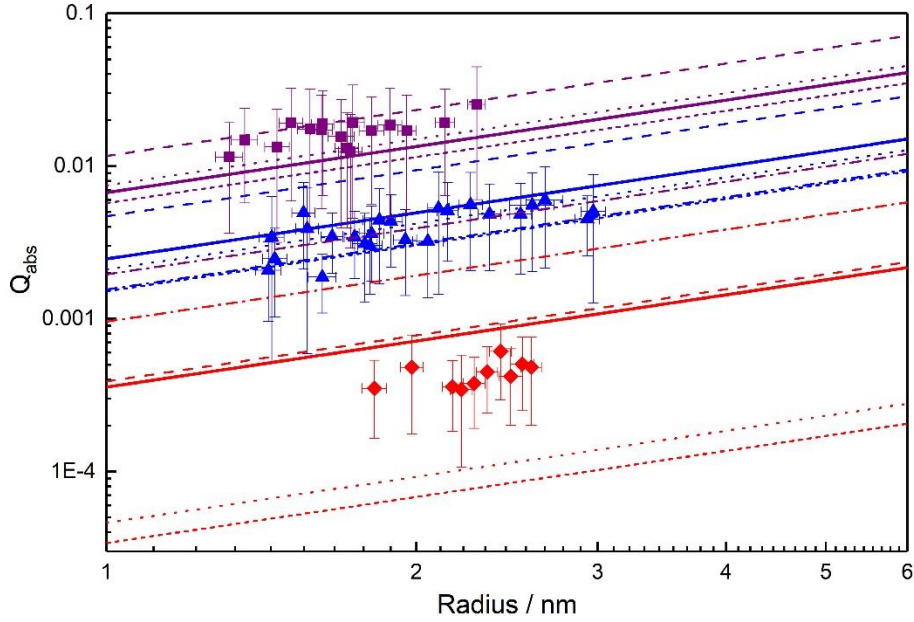
389

390 Figure 8. Absorption efficiencies for a range of particle sizes at three different wavelengths: 405 nm
391 (purple), 488 nm (blue) and 660 nm (red). Also shown are the literature data for hematite particles from
392 Querry (long dash), Hsu and Matijevic (short dash), Bedidi and Cervelle (dot dash), Longtin et al. (dotted)
393 and the average (bold lines).

394

395 In order to model the PAFS data, at each of the three wavelengths studied with the
396 MICE/TRAPS (405, 488 and 660 nm), a range of best-fit complex RIs (equation E4, where n and
397 k are the real and imaginary parts, respectively) was established by iterating over a range of
398 possible RIs and calculating absorption cross sections for each real-imaginary pair using Mie
399 theory. The indices resulting in the smallest normalized square difference ($d_{abs,\lambda}$, E5) between the
400 measured ($C_{abs,exp}$) and calculated ($C_{abs,calc}$) absorption cross section gave the best-fit RIs to the
401 absorption data at that wavelength (Figure 9).

402 E4 $$\underline{n} = n + ik$$

403 E5 $$d_{abs,\lambda} = ((C_{abs,exp} - C_{abs,calc})/C_{abs,exp})^2$$

404 By neglecting the scattering component in the absorption-dominated OD, the extinction cross
405 sections measured in the PAFS could be approximated using the absorption cross sections
406 measured in the MICE/TRAPS. This enabled a best-fit primary particle concentration to be
407 determined for the PAFS particles, using data from the two wavelengths at which the measured
408 extinction was above the detection limit (405 nm and 488 nm). Using the best-fit complex RIs
409 from the MICE/TRAPS data, the PAFS extinction was calculated using the RDG approximation
410 for a range of primary particle concentrations. At each wavelength (405 or 488 nm), the
411 normalized square difference between the measured and calculated extinction cross sections was
412 calculated for each concentration ($\delta_{ext,\lambda}$, equation E6, where $C_{ext,exp}$ and $C_{ext,calc}$ are the
413 experimental and calculated extinction cross sections, respectively). The $\delta_{ext,\lambda}$ values for the two
414 wavelengths were summed to derive χ^2_{ext} (equation E7) and the concentration resulting in the

415 smallest χ^2_{ext} value gave the best-fit primary particle concentration, generating the best match to
416 the measured extinction over the two wavelengths.

417 Using this best-fit primary particle concentration of 3.14×10^{10} cm^{-3}, $\delta_{ext,\lambda}$ was calculated for a
418 range of complex RIs at 405 and 488 nm, with the indices giving the smallest $\delta_{ext,\lambda}$ value
419 defining the best-fit to the extinction data at each wavelength (Figure 9). The final best-fit RIs at
420 each wavelength, fitting both the absorption and extinction data, were those that generated the
421 minimum combined δ value (δ_λ, equation E8). At 660 nm, the final best-fit RIs used were those
422 which best fit the absorption (gave the minimum $\delta_{abs,\lambda}$).

423 E6
$$\delta_{ext,\lambda} = ((C_{ext,exp} - C_{ext,calc})/C_{ext,exp})^2$$

424 E7
$$\chi^2_{ext} = \Sigma\, \delta_{ext,\lambda}$$

425 E8
$$\delta_\lambda = (\delta d_{ext,\lambda} - \delta_{abs,\lambda})^2$$
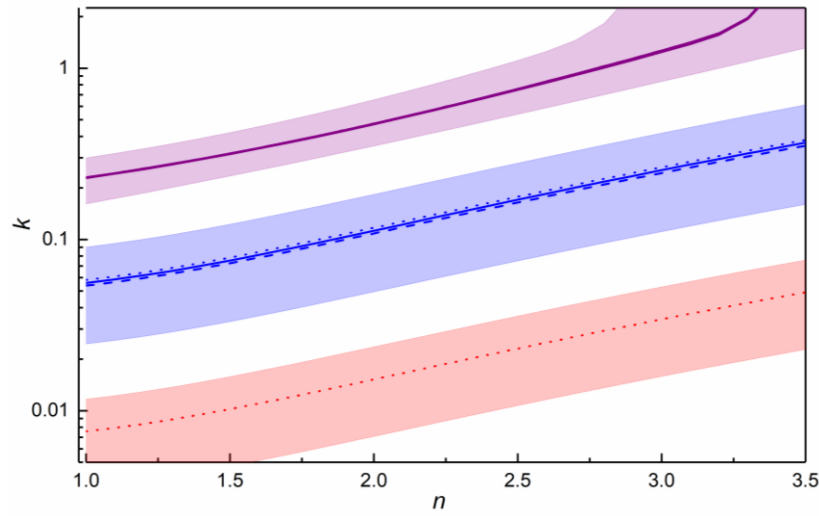
426

427 Figure 9. Best-fit RIs k and n for data at 405 nm (purple), 488 nm (blue) and 660 nm (red), for absorption
428 (dotted lines), extinction (dashed lines) and the combination (solid lines). Shaded regions indicate where
429 the resulting absorption and extinction cross sections are within experimental error for both experiments.

430 As it is possible to reproduce the measured absorption and extinction data at each wavelength
431 using multiple different combinations of RIs, it is not possible to identify a unique solution for
432 the wavelength dependence of these parameters. However, one way forward is first to select the
433 wavelength dependence of the real RIs, which have a much smaller impact on the extinction
434 cross section than the imaginary RIs in the absorption-dominated regime. The literature data for
435 hematite from Hsu and Matijevic (1985), Longtin et al. (1988) and Querry (1985) very
436 satisfactorily fit the experimental data across the whole wavelength range within experimental
437 errors using the RDG approximation (Figure 6, red line). Thus, for the unidentified particles an
438 average of the real RIs from these data was used (Figure 10, top panel). Using these real RIs at
439 405, 488 and 660 nm, the imaginary RI at each wavelength was selected from the best-fit data
440 (Table S1). The wavelength dependence was then determined by fitting an exponential decay
441 function through the three values (Figure 10, top panel, Table S1). The wavelength dependent
442 optical densities calculated using these RIs are shown in Figure 10 (bottom panel). At 405, 488
443 and 660 nm the calculated absorption efficiencies for a 1.65 nm particle are 1.59×10^{-2}, $3.19 \times$

444 10^{-3} and 3.19×10^{-4} respectively, compared to the experimentally determined values of $(1.60 \pm$
445 $1.15) \times 10^{-2}$, $(3.31 \pm 1.92) \times 10^{-3}$ and $(3.19 \pm 1.73) \times 10^{-4}$.
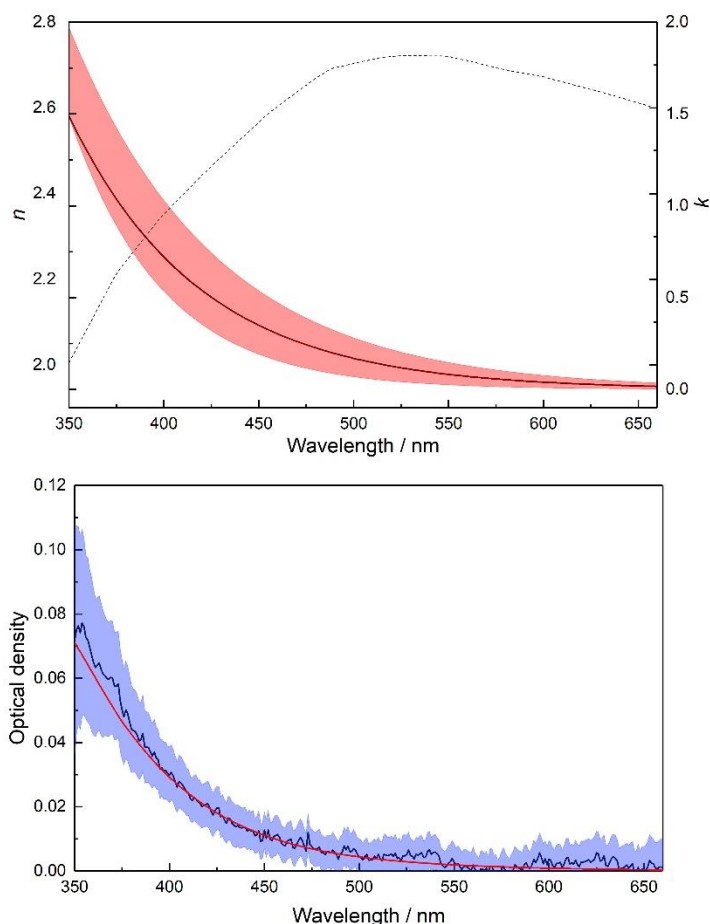
446
447 Figure 10. Top panel: Real (n) and imaginary (k) RIs for maghemite particles (dashed and solid lines,
448 respectively) with the uncertainty in k indicated with red shading. Bottom panel: Experimental OD (blue)
449 and the calculated OD (red) using the wavelength dependent RIs for maghemite particles.

450

451 **4. Conclusions**

452 Wavelength-dependent complex RIs have been derived for iron oxide meteoric smoke analogues
453 generated under atmospherically relevant conditions using two different experimental systems.
454 Analysis of particles collected from both experiments suggested a maghemite-like composition
455 to be most likely, although, for the particles produced in the PAFS, a magnetite-like composition
456 could not be definitively ruled out. Assuming the PAFS particles were indeed maghemite-like,
457 data from the two experiments was combined using an iteration procedure to determine 'best-fit'
458 complex RIs that replicate both experimental datasets at 405 nm and 488 nm, and the absorption
459 data at 660 nm. Values for the real RIs from the literature that generated the closest match to the
460 measured extinction data (using the RDG approximation for 1.65 nm particles) were used with
461 the best-fit data to determine the imaginary RIs at wavelengths between 350 and 660 nm.

462

463 Despite a number of iron oxides being considered as some of the most probable constituents of
464 meteoric smoke, maghemite particles have not previously been investigated due to a lack of RIs
465 available in the literature. Note that the production of maghemite-like particles in the laboratory
466 using very different experimental conditions demonstrates the potential importance of this species
467 in the atmosphere. Mesospheric metal chemistry leads to the formation of gas-phase precursors to
468 MSPs such as iron oxides and hydroxides. The particle production method used in the PAFS
469 mimics this: UV photolysis of $Fe(CO)_5$ leads to the formation of gas-phase Fe, which reacts with
470 O_3 present in the system to form oxides such as FeO, FeO_2 and FeO_3. Particles were then allowed
471 to freely agglomerate in the presence of O_2 and O_3 – as they would in the atmosphere. Since the
472 two experiments use a different iron precursors ($Fe(CO)_5$ and $Fe(C_2H_5)_2$), the choice of precursor
473 does not appear to be a significant factor affecting the composition of particles formed. The PAFS
474 operates at standard atmospheric pressure, and the MICE-TRAPS particles are produced at a much
475 lower pressure of ~60 mbar. Although still higher than in the upper mesosphere, the formation of
476 similar particles in the two experiments suggests that pressure does not significantly change the
477 particle properties. Lastly, in the PAFS experiments the $O_3:O_2$ ratio used is ~$10^3 \times$ higher than in
478 the atmosphere. However, the particles in the MICE-TRAPS apparatus are produced in the
479 presence of O_2 only, and still form maghemite-like particles. As mentioned in the Introduction, the
480 most likely candidates for smoke particles are iron oxides and silicates, but it is not known whether
481 these occur in a single phase or separate distinct phases. For this reason, there is a need for further
482 studies on the optical properties of maghemite.

483 The present study also demonstrates that the RDG approximation is more appropriate than Mie
484 theory to model the optical properties of fractal-like MSPs, since Mie theory over-predicts the
485 optical extinction by at least an order of magnitude across the wavelength range studied. This
486 supports the earlier work of Saunders et al. (2007) and is important since current studies with the
487 SOFIE satellite calculate MSP extinction using Mie theory for a distribution of spherical
488 particles (Hervig et al., 2017). Nevertheless, the fact that the derived complex RIs generated
489 good fits to both the absorption and extinction produced by crystalline and amorphous particles
490 in the MICE-TRAPS and PAFS experiments, respectively, lends confidence to the idea that it is
491 appropriate to use the RIs for bulk (crystalline) species to represent amorphous MSPs for the
492 purposes of their characterisation.

493 Though the complex RIs derived for the particles do not represent a unique solution to the
494 wavelength dependence across the wavelength range studied, they provide good fits to both the
495 experimental extinction and absorption in the two experiments. As such, since the important
496 parameter for MSP characterization in the atmosphere is the particle extinction, these RIs should
497 be applicable across this wavelength range (using different combinations of best-fit RIs incurs an
498 error of < 0.4 % in the particle extinction at 405, 488 and 660 nm). However, in order for these
499 RIs to be used with data from the SOFIE satellite, the wavelength range would need to be extended
500 further into both ultra-violet and infra-red wavelengths. With the current data, although
501 extrapolation to a wavelength of 330 nm may be feasible, it is not possible to extrapolate to the
502 other wavelengths currently used for SOFIE analysis (867 and 1037 nm); the difference in
503 wavelength is too great, given the unpredictable variation in RIs usually observed across wide
504 wavelength ranges. Nevertheless, the RIs could be used in global climate models to probe the
505 optical properties of meteoric smoke and make comparisons to observations.

506

Author contribution

The PAFS experiments were designed by TA, AJ and JP, and carried out by TA, who also performed the data analysis. The photochemical model was designed and written by TA, based on code written by JB. The MICE/TRAPS experiments were designed by MN, DD and TL. Experiments were carried out by MN and TA. MN performed the data analysis. TA prepared the manuscript with contributions from all co-authors. DD, JP and TL supervised the project.

Acknowledgements

This work was supported by the UK National Environment Research Council (NERC). TA has a research studentship funded by the NERC SPHERES doctoral training program, which included funding for a research placement at the Karlsruhe Institute of Technology (KIT), Institute of Meteorology and Climate Research. We would also like to thank Andy Brown at the Leeds Electron Microscopy and Spectroscopy Centre (LEMAS) for his invaluable help with the TEM, EDX and EELS analysis, and for providing data for the iron oxide standards. We thank Prof. Dwayne Heard for the loan of the SMPS instrument. The refractive index data and $Fe(CO)_5$ absorption spectrum are archived at the Leeds University PETAL (PetaByte Environmental Tape Archive and Library; http://www.see.leeds.ac.uk/business-and-consultation/facilities/petabyte-environmental-tape-archiveand-library-petal/) and are available upon request to JMCP.

References

Bedidi, A., and Cervelle, B.: Light scattering by spherical particles with hematite and goethitelike optical properties: Effect of water impregnation, J. Geophys. Res.-Solid Earth, 98, 11941-11952, 10.1029/93JB00188, 1993.

Brown, A. P., Moore, R. G. C., Evans, S., and Brydson, R.: Characterisation of iron oxide nanoparticles using EELS, Conference: Conference of the Electron-Microscopy-and Analysis-Group, 255-258 pp., 2001.

Brown, A. P., Hillier, S., and Brydson, R. M. D.: Quantification of Fe-oxidation state in mixed valence

minerals: a geochemical application of EELS revisited, Journal of Physics: Conference Series, 902, 10.1088/1742-6596/902/1/012016, 2017.

David, B., Pizurova, N., Schneeweiss, O., Santavá, E., Kudrle, V., and Jašek, O.: Gamma-Fe_2O_3 Nanopowders Synthesized in Microwave Plasma and Extraordinarily Strong Temperature Influence on Their Mossbauer Spectra, J. Nanosci. Nanotech., 12, 9277-9285, 10.1166/jnn.2012.6767, 2012.

DeCarlo, P. F., Slowik, J. G., Worsnop, D. R., Davidovits, P., and Jimenez, J. L.: Particle morphology and density characterization by combined mobility and aerodynamic diameter

543   measurements. Part 1: Theory, Aerosol Sci. Tech., 38, 1185-1205, 10.1080/027868290903907,
544   2004.

545   Duft, D., Nachbar, M., Eritt, M., and Leisner, T.: A Linear Trap for Studying the Interaction of
546   Nanoparticles with Supersaturated Vapors, Aerosol Sci. Tech., 49, 682-690,
547   10.1080/02786826.2015.1063583, 2015.

548   Fontijn, W. F. J., vanderZaag, P. J., Devillers, M. A. C., Brabers, V. A. M., and Metselaar, R.:
549   Optical and magneto-optical polar Kerr spectra of Fe_3O_4 and Mg^{2+}- or Al^{3+}-substituted Fe_3O_4,
550   Phys. Rev. B, 56, 5432-5442, 10.1103/PhysRevB.56.5432, 1997.

551   Henning, T., and Mutschke, H.: Low-temperature infrared properties of cosmic dust analogues,
552   Astron. Astrophys., 327, 743-754, 1997.

553   Hervig, M. E., Brooke, J. S. A., Feng, W., Bardeen, C. G., and Plane, J. M. C.: Constraints on
554   Meteoric Smoke Composition and Meteoric Influx Using SOFIE Observations With Models, J.
555   Geophys. Res.-Atmos., 122, 13495-13505, 10.1002/2017JD027657, 2017.

556   Hsu, W. P., and Matijevic, E.: Optical properties of monodispersed hematite hydrosols, Appl.
557   Opt., 24, 1623-1630, 10.1364/AO.24.001623, 1985.

558   Huffman, D. R., and Stapp, J. L.: Optical Measurements on Solids of Possible Interstellar
559   Importance, in: Interstellar Dust and Related Topics, edited by: Greenberg, J. M., and Van De
560   Hulst, H. C., Springer Netherlands, Dordrecht, 297-301, 1973.

561   Jacobson, M. Z.: Fundamentals of Atmospheric Modeling, 2nd edn., Cambridge Univ. Press,
562   New York, 2005.

563   Jain, P. K., Xiao, Y. H., Walsworth, R., and Cohen, A. E.: Surface Plasmon Resonance
564   Enhanced Magneto-Optics (SuPREMO): Faraday Rotation Enhancement in Gold-Coated Iron
565   Oxide Nanocrystals, Nano Lett., 9, 1644-1650, 10.1021/nl900007k, 2009.

566   Longtin, D. R., Shettle, E. P., Hummel, J. r., and , and Pryce, J. D.: A Wind Dependent Desert
567   Aerosol Model: Refractive Properties, Air Force Syst. Command, Air Force Geophys. Lab.,
568   Hanscom Air Force Base, USA, 115 pp., 1988.

569   Meinen, J., Khasminskaya, S., Eritt, M., Leisner, T., Antonsson, E., Langer, B., and Ruhl, E.:
570   Core level photoionization on free sub-10-nm nanoparticles using synchrotron radiation, Rev.
571   Sci. Instr., 81, art. no.: 085107, 10.1063/1.3475154, 2010a.

572   Meinen, J., Khasminskaya, S., Ruhl, E., Baumann, W., and Leisner, T.: The TRAPS Apparatus:
573   Enhancing Target Density of Nanoparticle Beams in Vacuum for X-ray and Optical
574   Spectroscopy, Aerosol Sci. Tech., 44, 316-328, 10.1080/02786821003639692, 2010b.

575   Nachbar, M., Duft, D., Mangan, T. P., Martin, J. C. G., Plane, J. M. C., and Leisner, T.:
576   Laboratory measurements of heterogeneous CO_2 ice nucleation on nanoparticles under
577   conditions relevant to the Martian mesosphere, J. Geophys. Res.-Planets, 121, 753-769,
578   10.1002/2015JE004978 2016.

579 Nachbar, M., Duft, D., Kiselev, A., and Leisner, T.: Composition, Mixing State and Water
580 Affinity of Meteoric Smoke Analogue Nanoparticles Produced in a Non-Thermal Microwave
581 Plasma Source, Zeitschrift für Physikalische Chemie, 232, 635-648, 2018a.

582 Nachbar, M., Duft, D., and Leisner, T.: The vapor pressure over nano-crystalline ice, Atmos.
583 Chem. Phys., 18, 3419-3431, 10.5194/acp-18-3419-2018, 2018b.

584 Nachbar, M., Wilms, H., Duft, D., Aylett, T., Kitajima, K., Majima, T., Plane, J. M. C., Rapp,
585 M., and Leisner, T.: The impact of solar radiation on polar mesospheric ice particle formation,
586 Atmos. Chem. Phys. Discuss., in review, 10.5194/acp-2018-1032, 2018c.

587 Navrotsky, A., Mazeina, L., and Majzlan, J.: Size-driven structural and thermodynamic
588 complexity in iron oxides, Science, 319, 1635-1638, 10.1126/science.1148614, 2008.

589 Plane, J. M. C., Feng, W., and Dawkins, E. C. M.: The Mesosphere and Metals: Chemistry and
590 Changes, Chem. Rev., 115, 4497-4541, 10.1021/cr500501m, 2015.

591 Querry, M. R.: Optical Constants, Contractor report, , US Army Chemical Research,
592 Development and Engineering Center (CRDC), Aberdeen Proving Ground, MD, USA, 415 pp.,
593 1985.

594 Rapp, M., Strelnikova, I., Strelnikov, B., Hoffmann, P., Friedrich, M., Gumbel, J., Megner, L.,
595 Hoppe, U. P., Robertson, S., Knappmiller, S., Wolff, M., and Marsh, D. R.: Rocket-borne in situ
596 measurements of meteor smoke: Charging properties and implications for seasonal variation, J.
597 Geophys. Res.-Atmos., 115, art. no.: D00I16, 10.1029/2009JD012725, 2010.

598 Rapp, M., Plane, J. M. C., Strelnikov, B., Stober, G., Ernst, S., Hedin, J., Friedrich, M., and
599 Hoppe, U. P.: In situ observations of meteor smoke particles (MSP) during the Geminids 2010:
600 constraints on MSP size, work function and composition, Ann. Geophys., 30, 1661-1673,
601 10.5194/angeo-30-1661-2012, 2012.

602 Saunders, R. W., and Plane, J. M. C.: A laboratory study of meteor smoke analogues:
603 Composition, optical properties and growth kinetics, J. Atmos. Solar-Terr. Phys., 68, 2182-2202,
604 10.1016/j.jastp.2006.09.006, 2006.

605 Saunders, R. W., Forster, P. M., and Plane, J. M. C.: Potential climatic effects of meteoric smoke
606 in the Earth's paleo-atmosphere, 34, 10.1029/2007gl029648, 2007.

607 Saunders, R. W., and Plane, J. M. C.: The formation and growth of Fe_2O_3 nanoparticles from the
608 photo-oxidation of iron pentacarbonyl, J. Aerosol Sci., 41, 475-489,
609 10.1016/j.jaerosci.2010.02.009, 2010.

610 Saunders, R. W., and Plane, J. M. C.: A photo-chemical method for the production of olivine
611 nanoparticles as cosmic dust analogues, Icarus, 212, 373-382, 10.1016/j.icarus.2010.12.019,
612 2011.

613   Self, D. E., and Plane, J. M. C.: A kinetic study of the reactions of iron oxides and hydroxides
614   relevant to the chemistry of iron in the upper mesosphere, Phys Chem Chem Phys, 5, 1407-1418,
615   10.1039/b211900e, 2003.

616   Sorensen, C. M.: Light Scattering by Fractal Aggregates: A Review, Aerosol Sci. Tech., 35, 648-
617   687, 10.1080/02786820117868, 2001.

618   Tang, J., Myers, M., Bosnick, K. A., and Brus, L. E.: Magnetite Fe_3O_4 nanocrystals:
619   Spectroscopic observation of aqueous oxidation kinetics, J. Phys. Chem. B, 107, 7501-7506,
620   10.1021/jp027048e, 2003.

621